Journal of
Materials Chemistry C

ROYAL SOCIETY
OF CHEMISTRY

PAPER

View Article Online
View Journal | View Issue

Check for updates

Cite this: *J. Mater. Chem. C*, 2020, **8**, 3374

Balanced strain-dependent carrier dynamics in flexible organic–inorganic hybrid perovskites†

Cheng Wang,[a] Lin Ma,*[a] Deqiang Guo,[a] Xin Zhao,[a] Zilin Zhou,[a] Dabin Lin,[a] Fangteng Zhang,[a] Weiren Zhao,[a] Jiahua Zhang[b] and Zhaogang Nie*[a]

Received 21st October 2019,
Accepted 17th January 2020

DOI: 10.1039/c9tc05763c

rsc.li/materials-c

Carrier dynamics of flexible organic–inorganic hybrid perovskite $CH_3NH_3PbI_3$ ($MAPbI_3$) films under various strains after photoexcitation were characterized by using time-resolved spectroscopy. The time-resolved photoluminescence study demonstrated that the charge carrier lifetime increases with increasing tensile strain, while it decreases with increasing compressive strain. This balanced optical response to tensile and compressive strains sheds light on the origin of ultra-stable optoelectric properties and overall film flexibility performance, which is further corroborated by transient absorption measurements. Moreover, the stability of flexible $MAPbI_3$ films was enhanced by doping a tiny amount of rubrene molecules in an $MAPbI_3$ precursor, without influencing the film structure or carrier dynamics. Our study provides new insights into the outstanding optoelectric properties and flexibility of the films and offers a novel method to improve the stability of organic–inorganic hybrid perovskite based flexible devices.

1 Introduction

Over the past decade, organic–inorganic hybrid perovskites (OIHPs) have been extensively employed as outstanding light absorbers in optoelectronic devices such as photovoltaics,[1] light-emitting diodes,[2] photodetectors,[3] lasers,[4] and radiation detectors,[5] due to their inherent merits of large absorption coefficient, high carrier mobility, tunable band gap and long carrier diffusion length.[4,6–8] The highest power conversion efficiency (PCE) of OIHP-based all-perovskite multi-junction solar cells that has been achieved is 26.7%.[9] Apart from rigid planar devices, the low-temperature solution fabrication of OIHPs enables an easy and scalable film deposition on flexible substrates achieving flexible optoelectronic devices with high mechanical flexibility and durability.[10–13] It is inevitable that tensile and compressive strains are induced by bending a flexible device in practical applications, such as portable and wearable electronics. Moreover, the OIHP film has a higher thermal expansion coefficient compared with quartz or glass, which will induce tensile strain in plane and compressive strain out of plane, respectively.[14] Therefore, even planar rigid OIHP films fabricated on quartz or glass substrates by existing methods are strained due to the thermal expansion mismatch between the perovskite film and substrates during a thermal annealing process.[14–16] Intriguingly, the residual or bending induced strains seem to have little influence on the performance of flexible OIHP devices. Previous studies have shown that flexible perovskite based solar cells can endure an ultimate small bending radius of less than 4 mm fabricated on polyethylene naphthalate (PEN),[11] 2 mm on polyethylene terephthalate (PET),[12] and 1 mm on polyethylenimine (PEI),[13] without showing significant performance degradation. Although electrical and mechanical properties of flexible perovskite-based devices have been intensively investigated, a study on the underlying mechanism of the ultra-stable optoelectronic properties under strain is still lacking.

In this work, carrier dynamics of a flexible $CH_3NH_3PbI_3$ ($MAPbI_3$) film deposited on a PET substrate under various tensile or compressive strains was studied using time-resolved spectroscopic techniques. The time-resolved photoluminescence (PL) measurements demonstrated that the charge carrier lifetime increases with increasing tensile strain, while it decreases with increasing compressive strain. This balanced optical response to tensile and compressive strains results in an ultra-stable overall film flexibility which is further verified by transient absorption measurements. In addition, enhanced film stability was achieved by doping a tiny amount of small organic molecules (rubrene) into the $MAPbI_3$ precursor without affecting the film structure or carrier lifetime. Our study reveals the balanced strain-dependent carrier dynamics in flexible OHIP films, and provides new insight towards understanding the mechanism of the ultra-stable flexibility of OHIP based devices.

---

[a] *School of Physics and Optoelectronic Engineering, Guangdong University of Technology, Guangzhou, China. E-mail: malin@gdut.edu.cn, zgnie@gdut.edu.cn*
[b] *State Key Laboratory of Luminescence and Applications, CIOMP, Chinese Academy of Sciences, Changchun, China*

† Electronic supplementary information (ESI) available. See DOI: 10.1039/c9tc05763c

2 Results and discussion

2.1 Tensile/compressive strain induced by convex/concave bending

A flexible $CH_3NH_3PbI_3$ ($MAPbI_3$) film was prepared on a polyethylene terephthalate (PET) substrate by a one-step spin-coating process (see Experimental section). The perovskite film thickness is around 300 nm, characterized by a step profiler. To systematically study the strain-dependent optical properties of the $MAPbI_3$ film, we designed a set of molds to bend the $MAPbI_3$ film with different bending radii as shown in Fig. S1 (ESI†). The strain applied on the substrate after bending is completely transferred to the $MAPbI_3$ film due to the large thickness difference between the perovskite film (300 nm) and the PET substrate (175 μm).[17] The applied tensile strain ε_1 to $MAPbI_3$ under convex bending (Fig. 1a) and compressive strain ε_2 under concave bending (Fig. 1b) are evaluated with eqn (1) and (2) as follows:[17,18]

$$\varepsilon_1 = \frac{h}{2r - h} \tag{1}$$

$$\varepsilon_2 = \frac{h}{2r + h} \tag{2}$$

where h is the total thickness of $MAPbI_3$ and the PET substrate and r is the bending curvature radius. To minimize the impact of inhomogeneity from film to film, we use the same perovskite film to perform a series of compressive/tensile strain measurements. Therefore, h is a constant which is equal to the sum of the thicknesses of perovskite (300 nm) and PET (175 μm). The strains applied and the corresponding bending radii are presented in Table S1 and Fig. S2 (ESI†). Fig. 1c shows the schematic diagram of strain change in a $MAPbI_3$ film during convex bending. $MAPbI_3$ has a relatively higher volumetric thermal expansion coefficient ($1.57–1.83 \times 10^{-4}$ K^{-1}), which is around three times larger than that of PET (5.4×10^{-5} K^{-1}).[14,16] Therefore, the as-deposited $MAPbI_3$ film is initially strained due to the thermal expansion coefficient mismatch between $MAPbI_3$ and the PET substrate. Moreover, the temperature gradient difference during thermal annealing causes a volume difference between the upper and lower layers in the film, resulting in compressive and tensile strain on the surface and bottom, respectively.[19,20] As the convex bending curvature increases, the residual compressive strain is first released, and tensile strain is introduced gradually, which leads to a strain evolution as shown in Fig. 1c. Scanning electron microscopy (SEM) images of a $MAPbI_3$ film under different tensile strain states *via* convex bending are shown in Fig. 1d. $MAPbI_3$ forms a network structure on the PET substrate, consistent with previous reports.[21–23] There is no obvious crack in the film under a strain of $\varepsilon_1 \leq 2\%$, while visible cracks appear gradually when $\varepsilon_1 > 2\%$.

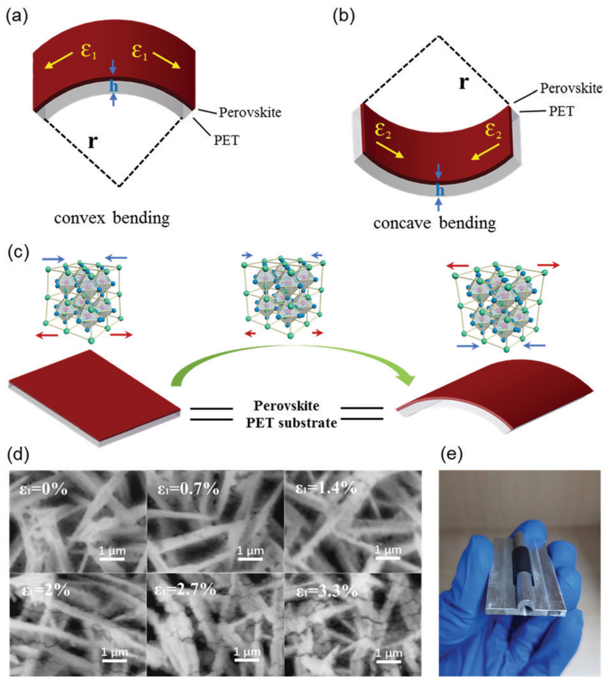

Fig. 1 Schematic diagrams of (a) convex, (b) concave bending and (c) lattice strain changes during a convex bending process. (d) SEM images of a $MAPbI_3$ film under different tensile strains. (e) The bending configuration corresponding to bending radius r = 2.75 mm (ε_1 = 3.3%).

2.2 Time-resolved photoluminescence (PL) characterization

In order to study the strain-dependent carrier dynamics in perovskite films, we recorded the time-resolved photoluminescence (PL) decays of flexible $MAPbI_3$ films under different bending configurations using a time-correlated single photon counting (TCSPC) technique. Since PL signals were collected from the front surface, the recorded PL lifetime reflects the carrier dynamics of the $MAPbI_3$ film under tensile strain (convex bending) or compressive strain (concave bending), respectively (as shown in the insets of Fig. 2a and b). The obtained PL decay traces

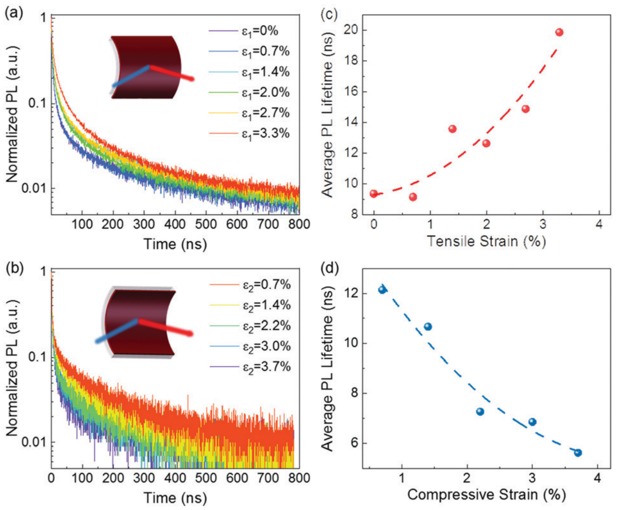

Fig. 2 Time-resolved PL kinetics at 760 nm of a $MAPbI_3$ film under (a) tensile strain (convex bending) and (b) compressive strain (concave bending) (each trace is normalized to its maximum intensity). Average PL lifetimes under various (c) tensile and (d) compressive strains (the dashed lines in (c) and (d) are to guide the eye).

under various tensile or compressive strains are presented in Fig. 2a and b. It is well known that free carriers are generated in perovskite after photoexcitation, therefore, a second order charge recombination together with a first order trap-limited recombination model is usually used to fit the PL decay curves.[24] Here, in order to qualitatively compare the carrier dynamics, we applied a three-exponential decay model to obtain satisfactory fits (eqn (S1), ESI†) and calculate the average PL lifetimes (eqn (S2), ESI†). Detailed fitting results are presented in Table S2 (ESI†). The average PL lifetimes *versus* tensile or compressive strains are plotted in Fig. 2c and d. There is an apparent trend that the PL lifetime increases with increasing tensile strain, while it decreases with increasing compressive strain. We attribute this to the carrier delocalization distance change induced by strains. To be more specific, tensile strain causes a lattice constant increment which increases the carrier delocalization distance, resulting in slower carrier recombination. However, compressive strain reduces the lattice constant which decreases the carrier delocalization distance and accelerates carrier recombination.

2.3 Transient absorption (TA) characterization

As mentioned above, time-resolved PL measurements were performed by collecting PL signals from the front surface of the film, which primarily offers carrier dynamics information from the surface of the $MAPbI_3$ film. However, the performance of a practical flexible device relies on the overall properties of the whole film. Therefore, we carried out femtosecond transient absorption (TA) spectroscopy measurements which record transmission changes of the whole film upon photoexcitation, and provide overall carrier dynamics responses to various strains. The normalized TA spectra at 2 ps after excitation of the $MAPbI_3$ film under various tensile strains are shown in Fig. 3a. There are two main features in the TA spectra: (i) a pronounced ground state bleaching (GSB) at 760 nm (1.35 eV), which is close to the optical bandgap of $MAPbI_3$; (ii) a photoinduced absorption (PIA) band at *ca.* 700 nm due to the absorption of photogenerated charge carriers. The GSB band undergoes subtle changes under different strains (Fig. 3b): under small tensile strains ($\varepsilon_1 \leq 1.4\%$), the GSB peak position shows a tiny blueshift with increasing strains (Fig. 3c). As the tensile strain further increases ($\varepsilon_1 \geq 2\%$), the GSB peak gradually red shifts. Al-Shami *et al.*[25] suggested that the band gap of $MAPbI_3$ decreases by increasing either positive (tensile) or negative (compressive) strains *via* first-principle calculations. Zhang *et al.*[26] reported that increasing the lattice constant under tensile strain resulted in an increasing bandgap. As mentioned above, the $MAPbI_3$ film is initially under compressive strain after thermal annealing. With increasing tensile strain *via* convex bending, the inherent compressive strain first releases and tensile strain is introduced gradually (Fig. 1c). Therefore, we can expect that the band gap will first increase and then decrease with increasing tensile strains applied in the $MAPbI_3$ film, which is in good agreement with our experimental results shown in Fig. 3c. Moreover, according to the turn point in Fig. 3c, we can infer that the residual compressive strain that remained in the $MAPbI_3$ film after thermal annealing (at 80 °C in our study) is around 1.4%. TA spectra of the $MAPbI_3$ film under different compressive strains are shown in Fig. S3 (ESI†). The GSB peak redshifts, *i.e.*, the band gap shows a decreasing trend as the compressive strain increases, consistent with the theoretical prediction.[26] TA kinetics at 760 nm under various tensile strains are shown in Fig. 3d. Intriguingly, unlike the apparent trend observed in time-resolved PL measurements, there is no noticeable change in the TA kinetics under different strain conditions. It indicates that the impacts on carrier dynamics induced by the tensile strain in the upper surface and the compressive strain in the bottom layer of the $MAPbI_3$ film compensate each other, resulting in overall stable carrier dynamics when measuring transmission of the whole film *via* TA spectroscopy. Thus, we conclude that the balanced optical responses of the $MAPbI_3$ film to tensile and compressive strains are responsible for the ultra-stable optoelectronic behaviors of perovskite-based devices reported previously.[27–29] As is known, the bending tolerance and bending stability are also important factors affecting the suitability of flexible devices for practical applications. Overbending a flexible film may cause a decline in optoelectronic properties. Although we have proven that carrier dynamics is stable under large strains in the flexible $MAPbI_3$ film, it is necessary to examine the durability after a large number of bending cycles. As shown in Fig. S4 (ESI†), we recorded the TA kinetic curves after bending a $MAPbI_3$ film for numerous cycles (up to 2000 cycles, bending radius $r = 1.1$ mm). The carrier lifetime showed a slight shortening after repeated bending, in agreement with the previous literature, which suggests that repeated bending has a certain attenuation effect on the efficiency of perovskite solar cells.[21,27,30] Therefore, efforts towards increasing the bending durability are still desired for further improving the durability of perovskite based flexible devices.

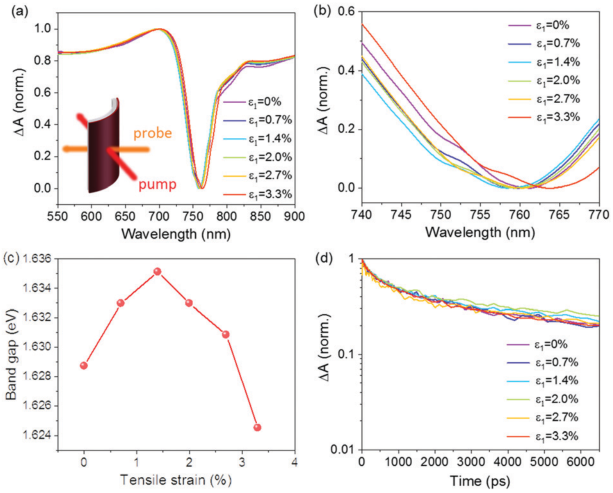

Fig. 3 (a) Transient absorption spectra of a $MAPbI_3$ film under different convex bending strains at 2 ps after excitation (λ_{pump} = 650 nm) and (b) the partial enlargement around the GSB peak. (c) Bandgap converted from the GSB peak position *versus* tensile strain. (d) The transient absorption decay traces (λ_{probe} = 760 nm) under different bending strains.

2.4 Stability enhancement *via* doping rubrene molecules

To further improve the stability of flexible perovskite films, we investigated the doping of small organic molecules into

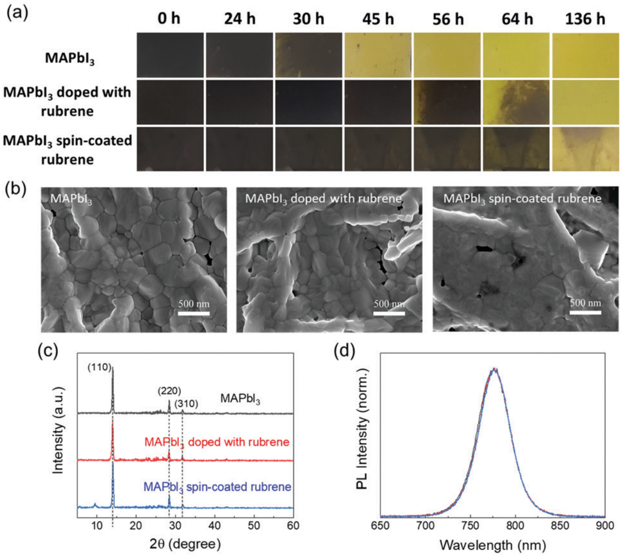

Fig. 4 (a) Film stabilities, (b) SEM images, (c) GIXRD patterns (background signals from PET substrates are subtracted) and (d) steady state PL spectra of pristine $MAPbI_3$, $MAPbI_3$ doped with rubrene (0.16 wt‰), and $MAPbI_3$ spin-coated rubrene on top.

$MAPbI_3$ films. Wei *et al.*[31] reported that the stability and device performance were significantly enhanced by spin coating rubrene molecules on top of $MAPbI_3$ films, owing to the cation–π interaction between rubrene and MA^+. Cong *et al.*[32] demonstrated that a rubrene underlayer not only promotes the grain growth, but also enhances the moisture resistance of perovskite films. Therefore, we chose rubrene molecules as the organic dopant. To simplify the fabrication procedure, we directly added a small amount of rubrene into the perovskite precursor solution and sequentially deposited the film *via* a one step spin-coating process. An $MAPbI_3$ film with rubrene spin-coated on top was also prepared for comparison. All film stabilities were recorded under extremely humid environmental conditions (average humidity $>85\%$, room light) without any encapsulation and deliberate protection from light illumination. The stabilities of $MAPbI_3$ films doped with rubrene at various concentrations are shown in Fig. S5 (ESI†). The best stability was obtained with a rubrene doping concentration of 0.16 wt‰. Additional fine tuning of the rubrene concentration could be beneficial for further improving the stability of the flexible perovskite film, while it is beyond the scope of this study. Film stabilities of pristine $MAPbI_3$, $MAPbI_3$ doped with rubrene, and $MAPbI_3$ spin-coated with rubrene on top deposited on PET substrates are presented in Fig. 4a. Compared to the pristine $MAPbI_3$ film which survives for only around 30 hours, $MAPbI_3$ doped with rubrene shows enhanced stability which kept most of the structure stable for 56 hours. This stability improvement can be attributed to the cation–π interaction between rubrene and MA^+ after doping rubrene into the $MAPbI_3$ structure.[31] $MAPbI_3$ spin coated with rubrene on top shows stability for slightly longer owing to the additional encapsulation of the top rubrene layer. SEM images of these three films are shown in Fig. 4b, which suggest that the grain boundaries are also reduced after doping or spin-coating rubrene molecules. The grazing incidence X-ray diffraction (GIXRD) patterns are plotted in Fig. 4c, with subtraction of the background signal from the PET substrate (original data are presented in Fig. S6, ESI†). There is no distinct difference in the XRD patterns of all films. All the films show strong diffraction peaks at 14.0°, 28.4° and 31.7° which correspond to the (110), (220) and (310) crystal planes of the tetragonal perovskite structure respectively.[33] The steady state PL spectra (Fig. 4d) also show no visible change, indicative of unaffected bandgaps. In addition, the response of carrier dynamics to strains was also measured for these three films (Fig. S7, ESI†). All films show similar kinetics under various tensile strains. Therefore, we conclude that the simple doping of a small number of rubrene molecules in $MAPbI_3$ improves the flexible perovskite film stability without influencing its structure, bandgap and charge carrier dynamics.

3 Conclusions

In summary, we investigated the origin of ultra-stable optoelectronic properties of flexible $MAPbI_3$ films by using time-resolved spectroscopic measurements. The charge carrier lifetime was demonstrated to increase with increasing tensile strain, while it decreased with increasing compressive strain as shown through a time-resolved photoluminescence study. This balanced optical response to tensile and compressive strains accounts for the ultra-stable optical response and outstanding overall film flexibility performance, further confirmed by transient absorption spectroscopy results. Enhanced film stability was achieved by doping a tiny amount of rubrene molecules into $MAPbI_3$, without influencing the film structure or carrier dynamics. Our study provides a new insight into the origin of the outstanding flexibility performance, and offers a novel simple method to improve the stability of flexible perovskite-based devices.

4 Experimental section

4.1 Materials

Methylammonium iodide (MAI, purity $\geq$ 99.5%) and lead iodide (PbI_2, purity $\geq$ 99.5%) were purchased from Xi'an Polymer Light Technology Corp. Rubrene powder was purchased from Ossila Ltd. The anhydrous *N*,*N*-dimethylformamide (DMF) was purchased from Sigma-Aldrich LLC., and the chlorobenzene (purity of 99.5%) was purchased from Macklin Inc. PET substrate was purchased from DuPont Teijin Films (Melinex 506, thickness of 175 μm). 66.3 mg of MAI and 188.7 mg of PbI_2 ($MAI : PbI_2$ molar ratio 1 : 1) were dissolved in 500 μL anhydrous DMF and stirred for 4 hours at 70 °C to achieve the perovskite precursor with a concentration of 35 wt%. Rubrene was dissolved in chlorobenzene (5 mg mL^{-1}) under stirring at 70 °C for 2 h to obtain a fully dissolved solution. A small amount (2.5, 5, or 10 μL) of the rubrene solution was then added into 100 μL of the above-prepared perovskite precursor to obtain the precursor solution with a rubrene doping concentration of 0.08, 0.16 or 0.32 wt‰. This solution was continually stirred at 70 °C for another 2 h to create an even mixture. Then 30 μL of the prepared solution was spin-coated on the PET substrate.

4.2 Perovskite flexible film fabrication

PET substrates were cleaned sequentially using Hellmanex III solution (1%), isopropanol and deionized water in an ultrasonic cleaner for 10 min respectively, and further treated with UV-ozone for 30 min. To prepare $MAPbI_3$ or $MAPbI_3$ doped with rubrene film, the precursor solution was spin-coated on the PET substrate at 4000 rpm for 30 s. For $MAPbI_3$ spin coated with rubrene on top, an additional 100 μL chlorobenzene solution dissolved rubrene (0.9 wt%) was spin-coated on the surface of the above spin-coated $MAPbI_3$ film at 4000 rpm for 20 s. All films were then annealed on a hot plate at 80 °C for 60 minutes. The above processes were carried out in a glovebox under a nitrogen atmosphere.

4.3 Steady state characterization

The film thickness was determined by a step profiler (ET-150, Kosaka). Grazing incidence X-ray diffraction measurements were performed by D/MAX-Ultima IV (Rigaku). Ultraviolet-visible (UV-Vis) absorption spectra were measured using a UV-3600 Plus spectrometer from SHIMADZU. In order to characterize the morphology change of perovskite films under strains, the $MAPbI_3$ film was placed on various molds with different bending radii. In order to fit the sizes of the molds, a lower resolution but larger sample store space Scanning Electron Microscope (SEM) (TM3030, Hitach) was used to record the SEM images shown in Fig. 1d. In Fig. 4b, we focus on the morphology change after doping rubrene, thus the perovskite film does not need bending by the molds, and thus a higher resolution (small sample space) field-emission SEM instrument (SU8220, Hitach, operated at 5.0 kV) was employed to resolve the fine grain structures in the perovskite film.

4.4 Time-resolved photoluminescence (PL)

Time-resolved PL measurements were conducted using the time-correlated single photon counting (TCSPC) module in a Fluorolog-3 spectrofluorometer (HORIBA). The excitation wavelength is 453 nm from a pulsed LED (pulse width: 1.4 ns).

4.5 Transient absorption (TA) spectroscopy

The TA spectra were collected using an amplified Ti:sapphire laser system (Solstice Ace, Spectra Physics), with an output of 800 nm at 1 kHz repetition rate, 35 fs pulse width, and output power of 6 W. Broadband pulses (500–1000 nm) are produced by spectrally broadening the output of 800 nm pulse in a neon-filled hollow-core fiber. Pulse compression by the chirped mirrors yields a pulse width of 8 fs. The broadband pulses were split into two beams by a beamsplitter. The weaker one was used as the probe beam, and the stronger one was used as the broadband excitation pump beam. The 650 nm pump pulse is generated by inserting a bandpass filter (center at 650 nm, 10 nm bandwidth) into the broadband pump pulse path. The pump energy of 650 nm (150 nJ per pulse) is in the linear absorption range to avoid nonlinear effects. A computer-controlled, piezo-driven high precision translation stage (Physik Instrumente) incorporated with a long travel range motorized stage (Newport) was placed in the pump beam arm to generate a time delay between the pump and probe pulses with 1 fs time delay precision and 8 ns time window.

Conflicts of interest

There are no conflicts to declare.

Acknowledgements

This work was supported by the National Natural Science Foundation of China (grant no. 11704079, 11874125, 11774071), the Science and Technology Program of Guangzhou (grant no. 201804010451 and 201904010104), the Guangdong University Students Science and Technology Innovation Training Special Fund (grant no. pdjh2019b0155), and the State Key Laboratory of Luminescence and Applications (grant no. SKLA-2019-08).

Notes and references

1 M. Liu, M. B. Johnston and H. J. Snaith, *Nature*, 2013, **501**, 395–398.

2 Z. K. Tan, R. S. Moghaddam, M. L. Lai, P. Docampo, R. Higler, F. Deschler, M. Price, A. Sadhanala, L. M. Pazos, D. Credgington, F. Hanusch, T. Bein, H. J. Snaith and R. H. Friend, *Nat. Nanotechnol.*, 2014, **9**, 687–692.

3 L. T. Dou, Y. Yang, J. B. You, Z. R. Hong, W. H. Chang, G. Li and Y. Yang, *Nat. Commun.*, 2014, **5**, 5404.

4 G. Xing, N. Mathews, S. S. Lim, N. Yantara, X. Liu, D. Sabba, M. Gratzel, S. Mhaisalkar and T. C. Sum, *Nat. Mater.*, 2014, **13**, 476–480.

5 S. Yakunin, D. N. Dirin, Y. Shynkarenko, V. Morad, I. Cherniukh, O. Nazarenko, D. Kreil, T. Nauser and M. V. Kovalenko, *Nat. Photonics*, 2016, **10**, 585–589.

6 M. A. Green, A. Ho-Baillie and H. J. Snaith, *Nat. Photonics*, 2014, **8**, 506–514.

7 C. C. Stoumpos, C. D. Malliakas and M. G. Kanatzidis, *Inorg. Chem.*, 2013, **52**, 9019–9038.

8 S. D. Stranks, G. E. Eperon, G. Grancini, C. Menelaou, M. J. Alcocer, T. Leijtens, L. M. Herz, A. Petrozza and H. J. Snaith, *Science*, 2013, **342**, 341–344.

9 D. P. McMeekin, S. Mahesh, N. K. Noel, M. T. Klug, J. Lim, J. H. Warby, J. M. Ball, L. M. Herz, M. B. Johnston and H. J. Snaith, *Joule*, 2019, **3**, 387–401.

10 N. Rolston, K. A. Bush, A. D. Printz, A. Gold-Parker, Y. C. Ding, M. F. Toney, M. D. McGehee and R. H. Dauskardt, *Adv. Energy Mater.*, 2018, **8**, 1802139.

11 B. J. Kim, D. H. Kim, Y. Y. Lee, H. W. Shin, G. S. Han, J. S. Hong, K. Mahmood, T. K. Ahn, Y. C. Joo, K. S. Hong, N. G. Park, S. Lee and H. S. Jung, *Energy Environ. Sci.*, 2015, **8**, 916–921.

12 Y. W. Li, L. Meng, Y. Yang, G. Y. Xu, Z. R. Hong, Q. Chen, J. B. You, G. Li, Y. Yang and Y. F. Li, *Nat. Commun.*, 2016, **7**, 10214.

13 S. M. Ahn, E. D. Jung, S. H. Kim, H. Kim, S. Lee, M. H. Song and J. Y. Kim, *Nano Lett.*, 2019, **19**, 3707–3715.

14 J. J. Zhao, Y. H. Deng, H. T. Wei, X. P. Zheng, Z. H. Yu, Y. C. Shao, J. E. Shield and J. S. Huang, *Sci. Adv.*, 2017, **3**, eaao5616.

15 K. A. Bush, N. Rolston, A. Gold-Parker, S. Manzoor, J. Hausele, Z. J. Yu, J. A. Raiford, R. Cheacharoen, Z. C. Holman, M. F. Toney, R. H. Dauskardt and M. D. McGehee, *ACS Energy Lett.*, 2018, **3**, 1225–1232.

16 T. J. Jacobsson, L. J. Schwan, M. Ottosson, A. Hagfeldt and T. Edvinsson, *Inorg. Chem.*, 2015, **54**, 10678–10685.

17 Z. H. Tang, B. M. Wang, H. L. Yang, X. Y. Xu, Y. W. Liu, D. D. Sun, L. X. Xia, Q. F. Zhan, B. Chen, M. H. Tang, Y. C. Zhou, J. L. Wang and R. W. Li, *Appl. Phys. Lett.*, 2014, **105**, 103504.

18 G. Dai, Q. Zhan, Y. Liu, H. Yang, X. Zhang, B. Chen and R.-W. Li, *Appl. Phys. Lett.*, 2012, **100**, 122407.

19 C. Zhu, X. X. Niu, Y. H. Fu, N. X. Li, C. Hu, Y. H. Chen, X. He, G. R. Na, P. F. Liu, H. C. Zai, Y. Ge, Y. Lu, X. X. Ke, Y. Bai, S. H. Yang, P. W. Chen, Y. J. Li, M. L. Sui, L. J. Zhang, H. P. Zhou and Q. Chen, *Nat. Commun.*, 2019, **10**, 815.

20 T. W. Jones, A. Osherov, M. Alsari, M. Sponseller, B. C. Duck, Y.-K. Jung, C. Settens, F. Niroui, R. Brenes, C. V. Stan, Y. Li, M. Abdi-Jalebi, N. Tamura, J. E. Macdonald, M. Burghammer, R. H. Friend, V. Bulović, A. Walsh, G. J. Wilson, S. Lilliu and S. D. Stranks, *Energy Environ. Sci.*, 2019, **12**, 596–606.

21 H. Xia, S. Tong, C. Zhang, C. Wang, J. Sun, J. He, J. Zhang, Y. Gao and J. Yang, *Appl. Phys. Lett.*, 2018, **112**, 233301.

22 A. Giuri, S. Masi, A. Listorti, G. Gigli, S. Colella, C. E. Corcione and A. Rizzo, *Nano Energy*, 2018, **54**, 400–408.

23 H. Deng, X. Yang, D. Dong, B. Li, D. Yang, S. Yuan, K. Qiao, Y. B. Cheng, J. Tang and H. Song, *Nano Lett.*, 2015, **15**, 7963–7969.

24 S. D. Stranks, V. M. Burlakov, T. Leijtens, J. M. Ball, A. Goriely and H. J. Snaith, *Phys. Rev. Appl.*, 2014, **2**, 034007.

25 A. Al-Shami, M. Lakhal, M. Hamedoun, A. El Kenz, A. Benyoussef, M. Loulidi, A. Ennaoui and O. Mounkachi, *Sol. Energy Mater. Sol. Cells*, 2018, **180**, 266–270.

26 L. Zhang, L. Wu, K. Wang and B. Zou, *Adv. Sci.*, 2019, **6**, 1801628.

27 C. Roldán-Carmona, O. Malinkiewicz, A. Soriano, G. Mínguez Espallargas, A. Garcia, P. Reinecke, T. Kroyer, M. I. Dar, M. K. Nazeeruddin and H. J. Bolink, *Energy Environ. Sci.*, 2014, **7**, 994–997.

28 L. Chen, X. Xie, Z. Liu and E.-C. Lee, *J. Mater. Chem. A*, 2017, **5**, 6974–6980.

29 L. Hou, Y. Wang, X. Liu, J. Wang, L. Wang, X. Li, G. Fu and S. Yang, *J. Mater. Chem. C*, 2018, **6**, 8770–8777.

30 H. Xiong, G. DeLuca, Y. C. Rui, B. X. Zhang, Y. G. Li, Q. H. Zhang, H. Z. Wang and E. Reichmanis, *ACS Appl. Mater. Interfaces*, 2018, **10**, 35385–35394.

31 D. Wei, F. Ma, R. Wang, S. Dou, P. Cui, H. Huang, J. Ji, E. Jia, X. Jia, S. Sajid, A. M. Elseman, L. Chu, Y. Li, B. Jiang, J. Qiao, Y. Yuan and M. Li, *Adv. Mater.*, 2018, **30**, e1707583.

32 S. Cong, H. Yang, Y. Lou, L. Han, Q. Yi, H. Wang, Y. Sun and G. Zou, *ACS Appl. Mater. Interfaces*, 2017, **9**, 2295–2300.

33 G. D. Niu, W. Z. Li, F. Q. Meng, L. D. Wang, H. P. Dong and Y. Qiu, *J. Mater. Chem. A*, 2014, **2**, 705–710.